Keyhole formation and collapse in plasma arc welding

H G Fan and R Kovacevic

Department of Mechanical Engineering, Southern Methodist University, Dallas, TX 75275, USA

Abstract. A mathematical model is developed to describe the heat transfer and fluid flow in stationary keyhole plasma arc welding. Using the volume of fluid method, the processes of heating, melting, collapsing and subsequent solidifying in the molten pool are dynamically studied. The predicted results have been compared with the experimental weld and keyhole shape. Using the LaserStrobe video system, the captured images of the upper surface of the weld pool are used to verify the predicted transient development of the weld pool. It is indicated that theoretical predictions and the experimental results are in close agreement.

Nomenclature

B_θ	azimuthal magnetic field
c_p	specific heat
f_L	liquid fraction
F	volume of fluid
g	gravitational acceleration
h	specific enthalpy
h_c	combined heat transfer coefficient at the surface
I	arc current
j_r, j_z	radial, axial current density
k	thermal conductivity
K	drag index in source term
K_b	Boltzmann's constant
K_{max}	maximum drag index
n, s	normal, tangential direction along surface
P	pressure
P_{arc}	arc pressure acting on top surface
$q_n(r)$	heat flux distribution normal to top surface
r, z	radial, axial coordinate
r_q, r_c	heat, current flux distribution radius
t	time
T	temperature
T_L	liquidus temperature
T_r	reference temperature
T_S	solidus temperature
u, w	radial, axial velocity
U	arc voltage
V_{arc}	velocity of arc plasma
V_n, V_s	normal, tangential velocity component at the molten pool surface
ΔH	latent heat of fusion
β	coefficient of thermal expansion
γ	surface tension
$d\gamma/dT$	temperature gradient of surface tension
η	arc efficiency
ε	radiation emissivity
μ	viscosity
μ_0	magnetic permeability
ρ	density of the molten pool
ρ_{arc}	density of the arc plasma
σ	electrical conductivity
τ_a	arc drag force acting on the top surface
ϕ	electrical potential

1. Introduction

In plasma arc welding (PAW), a constricted plasma arc is used as the concentrated energy source to melt the workpiece. Due to its high energy density and its high-velocity plasma jet, the PAW process can produce deeper weld penetrations, faster travel speeds and smaller thermal distortions than gas–tungsten arc welding [1]. PAW fusion modes can be categorized as either melt-in or keyhole. The keyhole mode is the primary attribute of PAW that makes it so attractive. In the keyhole-welding mode, as shown in figure 1, the plasma jet completely penetrates the weld pool, forming a symmetric, funnel-shaped cavity called a keyhole, and a similarly shaped liquid–solid metal phase boundary. Some mathematical models on the prediction of weld and keyhole shapes have been developed for electron beam and laser beam welding [2–4]. However, the mechanism of keyhole formation in these processes is different from that in the PAW process. In PAW the keyhole is produced and maintained mainly by the pressure of the arc plasma, rather than by the recoil pressure of the evaporating metal as in electron beam and laser welding. Up to the present time, the most comprehensive models of PAW are Rubinsky's two-dimensional (2D) and three-dimensional (3D) finite-element simulations [5, 6]. The 2D quasi-stationary model, which describes the weld pool flow and temperature fields with steady travel PAW, neglects surface tension effects and simplifies the pool geometry by assuming flat upper and lower free surfaces and a keyhole of constant radius. The developed 3D steady model is used
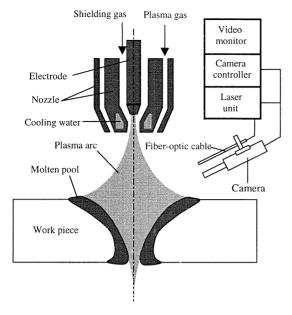
Figure 1. Schematic diagram of plasma arc and weld pool in keyhole PAW.

Table 1. Physical properties of the workpiece.

Symbol	Value	Symbol	Value
β	10^{-4} K^{-1}	ρ	7200 kg m^3
γ	1.2 N m^{-1}	μ_0	1.26×10^{-6} H m^{-1}
μ	0.006 kg m^{-1} s^{-1}	σ	7.7×10^5 mho m^{-1}
$d\gamma/dT$	10^{-4} N m^{-1} K^{-1}	ε	0.9
C_P	753 J kg^{-1} K^{-1}	ΔH	2.47×10^5 J kg^{-1}
T_l	1723 K	T_s	1523 K
k	20 W m^{-1} K^{-1}	K_{max}	10^4 s^{-1}

(3) the thermophysical properties, listed in table 1, are assumed to be constant;

(4) the fluid in the pool is driven by a combination of buoyancy, electromagnetic and surface tension forces; however, plasma jet shear is neglected; and

(5) the distribution of heat, current flux and pressure from the plasma arc are assumed to be Gaussian.

Based on these assumptions, the governing differential equations used to describe heat and fluid flow in the weld pool can be expressed as follows.

Equation of mass continuity:

$$\frac{1}{r}\frac{\partial(ru)}{\partial r} + \frac{\partial w}{\partial z} = 0. \tag{1}$$

Conservation of radial momentum:

$$\frac{\partial}{\partial t}(\rho u) + \frac{1}{r}\frac{\partial}{\partial r}\left(\rho r u^2 - \mu r \frac{\partial u}{\partial r}\right) + \frac{\partial}{\partial z}\left(\rho u w - \mu \frac{\partial u}{\partial z}\right)$$
$$= -\frac{\partial P}{\partial r} + \frac{1}{r}\frac{\partial}{\partial r}\left(\mu r \frac{\partial u}{\partial r}\right) - 2\mu\frac{u}{r^2} + \frac{\partial}{\partial z}\left(\mu \frac{\partial w}{\partial r}\right)$$
$$- j_z B_\theta - Ku. \tag{2}$$

Conservation of axial momentum:

$$\frac{\partial}{\partial t}(\rho w) + \frac{1}{r}\frac{\partial}{\partial r}\left(\rho r u w - \mu r \frac{\partial w}{\partial r}\right) + \frac{\partial}{\partial z}\left(\rho w^2 - \mu \frac{\partial w}{\partial z}\right)$$
$$= -\frac{\partial P}{\partial z} + \frac{1}{r}\frac{\partial}{\partial r}\left(\mu r \frac{\partial u}{\partial z}\right) + \frac{\partial}{\partial z}\left(\mu \frac{\partial w}{\partial z}\right)$$
$$- Kw + j_r B_\theta + \rho g \beta (T - T_r). \tag{3}$$

The temperature-dependent drag term which represents fluid flow in the mushy zone is incorporated into the momentum equation via $-Ku$ and $-Kw$ where

$$K = \begin{cases} 0 & T > T_l \\ K_{max}(T_l - T)/(T_l - T_s) & T_s \leqslant T \leqslant T_l \\ \infty & T < T_s \end{cases} \tag{4}$$

Conservation of energy:

$$\frac{\partial}{\partial t}(\rho h) + \frac{1}{r}\frac{\partial}{\partial r}\left(\rho r u h - r\frac{k}{C_p}\frac{\partial h}{\partial r}\right)$$
$$+ \frac{\partial}{\partial z}\left(\rho w h - \frac{k}{C_p}\frac{\partial h}{\partial z}\right)$$
$$= \frac{j_r^2 + j_z^2}{\sigma} - \Delta H \frac{\partial f_L}{\partial t}. \tag{5}$$

to predict the molten pool shape based on heat transfer and fluid flow, while the keyhole shape is assumed according to experimental results. So far, no theoretical study on the transient development of the keyhole shape in PAW has been found in the open literature.

In this paper, a 2D, transient model is developed to demonstrate the heat transfer and fluid flow in keyhole PAW. In the model, the weld pool surface is depressed by the arc pressure, and the fluid flow in the molten pool is induced by the surface tension gradient, electromagnetic force and the buoyancy force. The volume of fluid (VOF), modified to include heat transfer and the electromagnetic force, is used to track the transient deformed shape of the weld pool surface. The processes of heating, melting, collapsing and subsequent solidifying are simulated in the keyhole PAW; experiments are performed on 304 stainless-steel. The resultant weld and keyhole shapes have been compared with those predicted, and are in good agreement. In addition, the transient shape of the upper surface in the molten pool has been monitored by the use of a LaserStrobe video system in order to capture a video image of the process using intense lighting from a strobe illumination unit. The successive images are used to verify the transient process predicted by the presented model. This study may enhance our understanding of the heat transfer related phenomena during PAW.

2. Mathematical formulation

2.1. Governing equations

In order to simplify the mathematical model, or due to insufficient information, the following assumptions have been made:

(1) the welding process is restricted to stationary PAW, and the system is assumed to be axisymmetric;

(2) laminar flow is assumed;

In the energy equation, ohmic heating is considered. Latent heat of fusion is included by employing the liquid fraction, f_L, which is defined as follows:

$$f_L = \begin{cases} 1 & T > T_l \\ (T - T_s)/(T_l - T_s) & T_s \leqslant T \leqslant T_l \\ 0 & T < T_s \end{cases} \quad (6)$$

where T_l and T_s are the liquidus and solidus temperatures, respectively.

Conservation of electrical charge: In order to obtain the electromagnetic force terms in equations (2) and (3), the electric potential ϕ is calculated by solving the equation for current continuity:

$$\frac{1}{r}\frac{\partial}{\partial r}\left(\sigma r \frac{\partial \phi}{\partial r}\right) + \frac{\partial}{\partial z}\left(\sigma \frac{\partial \phi}{\partial z}\right) = 0 \quad (7)$$

and current density is calculated from Ohm's law,

$$j_r = -\sigma \frac{\partial \phi}{\partial r} \qquad j_z = -\sigma \frac{\partial \phi}{\partial z} \quad (8)$$

while the self-induced azimuthal magnetic field B_θ is derived from Ampere's law:

$$B_\theta = \frac{\mu_0}{r} \int_0^r j_z r \, \mathrm{d}r \quad (9)$$

2.2. Tracking of free surfaces

The moving free surface is tracked using a volume of fluid function, F, which represents the volume of fluid in the computational cell. The function F takes the value of one for the cell filled with the fluid, and takes the value of zero for the empty cell. If the cell is located on the free surface, the function F has a value between zero and one. The function F is governed by the equation [7]

$$\frac{\partial F}{\partial t} + \frac{1}{r}\frac{\partial}{\partial r}(ruF) + \frac{\partial}{\partial z}(wF) = 0. \quad (10)$$

2.3. Boundary conditions

2.3.1. Boundary conditions for momentum.
The boundary conditions needed to specify the fluid flow problem are:

(1) symmetry about the centreline,
(2) no slip at the solid boundaries,
(3) at the free surface, the plasma arc pressure P_{arc} can be approximated by

$$P_{arc} = P_{max} \exp\left(-\frac{3r^2}{r_p^2}\right) \quad (11)$$

where P_{max} is calculated by $\frac{1}{2}\rho_{arc} V_{arc}^2$, using values of ρ_{arc} and V_{arc} determined earlier [8]. Due to lack of experimental data concerning r_p; and because a PAW arc is a high-velocity, concentrated plasma jet, r_p is approximated as the orifice radius of the welding torch. The Marangoni force due to the

Table 2. PAW experimental conditions.

Welding current	100 A
Arc voltage	31 V
Shield flow rate	19 l min^{-1}
Plasma flow rate	2.5 l min^{-1}
Orifice diameter	3.2 mm
Torch standoff distance	5 mm

variation of the surface tension coefficient with temperature is described by [9]

$$\tau_s = \mu \frac{\partial V_s}{\partial n} = \frac{\mathrm{d}\gamma}{\mathrm{d}T}\frac{\partial T}{\partial s}. \quad (12)$$

The plasma arc pressure P_{arc} and the Marangoni force τ_s are included by adding source terms to the momentum equation. The method used is detailed in [10], which is called continuum surface force model.

2.3.2. Boundary conditions for thermal energy.
The boundary conditions pertaining to the heat-transfer problem are:

(1) symmetry about the axial centreline;
(2) at the free surface of the molten pool, the heat flux from the welding arc is approximated by

$$-k\frac{\partial T}{\partial n} = \frac{\eta U I}{2\pi r_q^2}\exp\left(-\frac{r^2}{2r_q^2}\right) - h_c(T - T_r) \quad (13)$$

where h_c is a combined heat transfer coefficient for the radiate and convective boundary expressed in the following equation [11]:

$$h_c = 24.1 \times 10^{-4}\varepsilon T^{1.61} \quad (14)$$

The heat flux from the arc plasma (equation (13)) is considered to be a source term of the energy conservation equation in the cells along the weld pool surface. The arc efficiency η is set as 0.55 according to an earlier experiment [12].

(3) the boundary conditions for the surfaces without heat input are expressed as

$$-k\frac{\partial T}{\partial n} = h_c(T - T_r). \quad (15)$$

2.3.3. Electric potential boundary conditions.
The boundary conditions concerning the electrical potential in the area of the molten pool are:

(1) symmetry about the centreline;
(2) an isopotential line ($\phi = 0$) is selected at the right wall because the right wall is far from the weld pool. $\partial\phi/\partial z = 0$ is set at the bottom wall; and
(3) at the free surface, the assumed Gaussian-type current flux is expressed by

$$-\sigma\frac{\partial\phi}{\partial n} = \frac{I}{2\pi r_c^2}\exp\left(-\frac{r^2}{2r_c^2}\right). \quad (16)$$
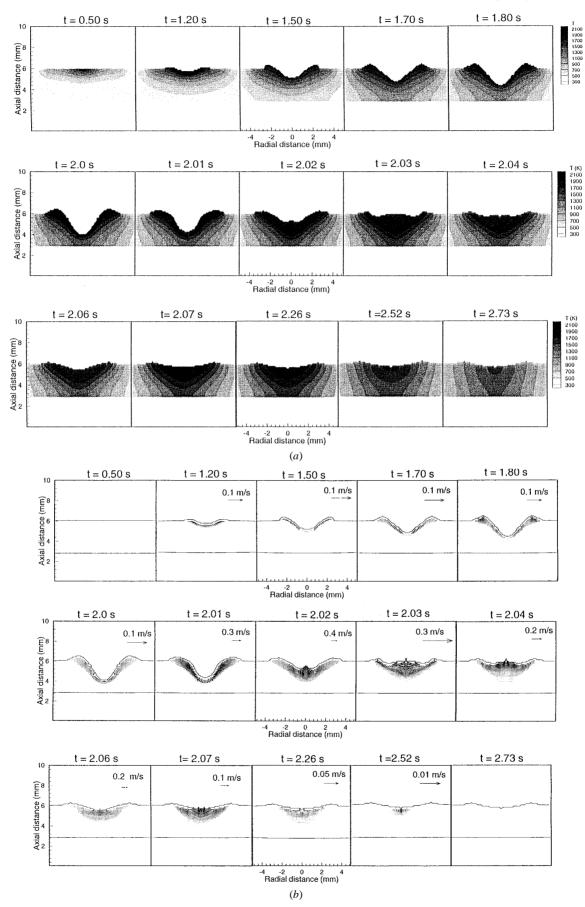
Figure 2. (*a*) Temperature distribution in the partially-penetrated weld and (*b*) velocity distribution in the partially-penetrated weld.
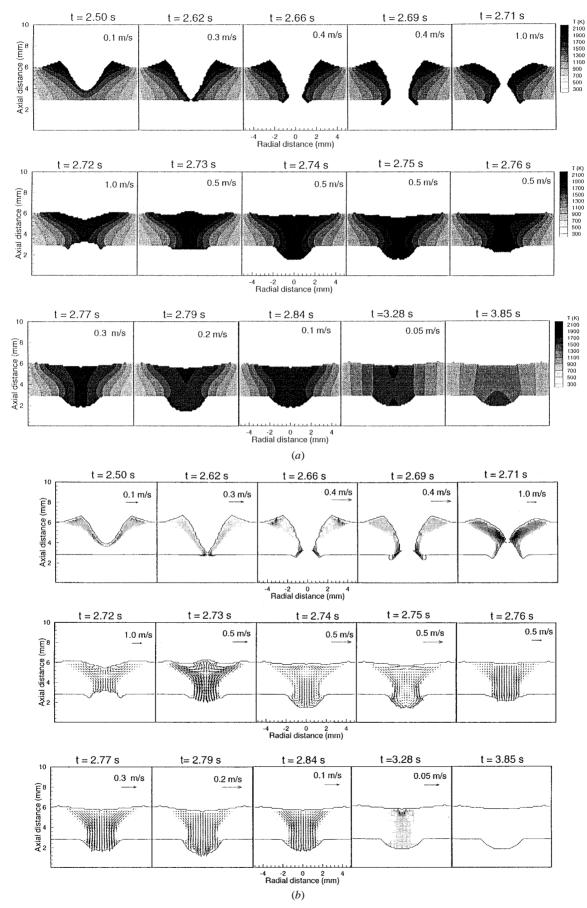
Figure 3. (*a*) Temperature distribution in the fully-penetrated weld and (*b*) velocity distribution in the fully-penetrated weld.

3. Experimental procedure

A power supply designed for PAW was used to make stationary spot welds on a 3.0 mm thick 304 stainless-steel plate. The welding was performed under a direct current, electrode negative condition. Pure argon was used as the shielding gas and the plasma gas. Other experimental conditions are given in table 2.
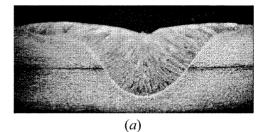
An ultra-high shutter speed vision system was used to simultaneously capture images of the weld pool from the front side of the workpiece in figure 1. The optical energy from the laser unit is transported to the viewing area with a fibre-optic cable. The system exploits the temporary situation by capturing an image with a special-purpose video camera head which is equipped with a charge-coupled device video sensor and a means for very high-speed electronic shuttering. The shutter is synchronized with the laser flash. The intensity of the laser illumination is much higher than that of the plasma. The camera unit is also equipped with a narrow-band optical filter to match the laser wavelength and further suppress the arc lighting. Using this vision system, the weld pool can be clearly observed and recorded on the video tape. The elapsed time can be shown on the video tape, which is also referred to as welding time in the experiment.
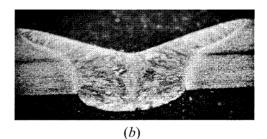
In the experiment, three cases were investigated: (1) a partial-penetration weld in which the welding arc is extinguished at the time $t = 2$ s, (2) a full-penetration weld in which the welding arc is extinguished as soon as the plasma arc is observed from the back side and (3) burn through in which the welding arc is extinguished if is observed to have burned through the metal.

4. Results and discussion

The development of the partially-penetrated weld pool in the keyhole mode PAW is presented in figure 2. The surface profile of the weld pool is determined by the arc pressure, gravitational force and the surface tension acting on the weld pool. In the partially-penetrated weld pool, the molten metal is pushed out by arc pressure; thus, the pool surface is depressed in the centre and humped at the pool boundary. It is shown that a hole with a V-shape cross section is formed because of the high-velocity, concentrated plasma arc. Since the plasma arc in the cone hole heats the base metal, the liquid–solid boundary has shown a similar V-shape.

The arc is extinguished at the time of 2 s. Influenced by gravity, the weld pool collapses. At $t = 2.01$ s in figure 2(b), the fluid is accelerated into the hole, causing the hole to fill. The weld pool oscillation is triggered by the impingement of inward flows at the centre of the weld pool. It is shown that the fluid moves upward after the impingement of inward flows, at $t = 2.02$ s. Affected by inertia, a hump, which overpasses the equilibrium, is formed at the top at $t = 2.03$ s. That is, part of the kinetic energy has been transferred to potential energy. Under the influence of the hydrostatic and surface tension forces, the fluid in the top begins to move downward at $t = 2.03$ s. It is shown that the downward flow is dominant in the weld pool at 2.04 s. Obviously, the downward flow will also pass the equilibrium of the above-mentioned forces due to inertia. Thus, it is seen that the fluid flow moves upward
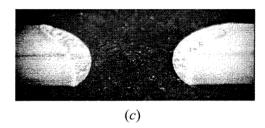

(a)

(b)

(c)

Figure 4. Experimentally observed weld fusion zone: (a) partial penetration, (b) full penetration and (c) keyhole shape after burnthrough.

again at $t = 2.07$ s. This loop will continue until equilibrium or solidification is achieved.

The corresponding temperature distribution is shown in figure 2(a). The keyhole develops so rapidly that the highest temperature appears near the top surface, although the heat flux from the arc plasma is higher in the centre of the weld pool. This is because the high temperature molten metal is always pushed toward the top surface by the plasma arc; furthermore, the central pool always approaches first, and is cooled by, the low-temperature base metal. After the collapse of the molten pool, the high-temperature molten metal from the top moves to the centre, resulting in a higher temperature at the centre. In the process of solidification, the heat loss is mainly from the heat conduction in the weld; thus, the higher temperature remains near the top surface.

As shown in figure 3, the molten pool is fully penetrated around $t = 2.62$ s. The molten metal is held by surface tension. In the newly developed bottom surface, surface tension also tends to form a shape that minimizes the surface energy. As shown in figure 3, a keyhole with a hyperbolic shape cross section is developed at $t = 2.69$ s.

The keyhole collapses at $t = 2.71$ s, after the arc is extinguished. The principle of the weld pool oscillation in the full-penetration weld is the same as that in the above-mentioned partial-penetration weld. However, the addition of a free bottom surface results in a more complex oscillation in the weld pool. At $t = 2.72$ s, the inward flows impinge in the centre; thus, the fluid at the top moves upward and the fluid at the bottom moves downward. At $t = 2.73$ s, the top part of the pool, which overpasses the equilibrium, begins
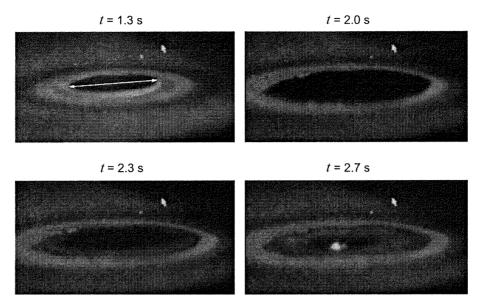
$t = 1.3$ s $t = 2.0$ s

$t = 2.3$ s $t = 2.7$ s

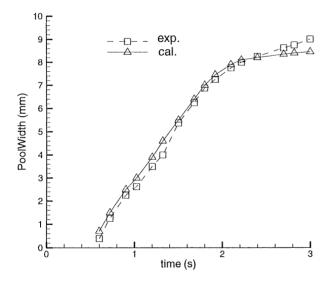**Figure 5.** Images of the top surface in the partially-penetrated weld.

Figure 6. Comparison of calculated and experimental weld pool width.

to move downward. The downward flow is dominant in the weld pool at $t = 2.74$ s. Meanwhile, influenced by surface tension, the flow direction of the bottom part begins to change. It is obvious that the upward flow from the bottom will affect the flow in the top. Then, the upward flow is dominant at $t = 2.76$ s. At $t = 2.77$ s and 2.79 s, it is seen that the flow directions in the weld pool change again. The weld pool oscillation will continue until equilibrium is achieved or the weld pool is solidified.

Figure 3(a) describes the temperature distribution of the fully-penetrated weld. After the collapse of the keyhole, a higher temperature distribution at the centre is shown. In the process of solidification, the higher-temperature fluid remains near to the top and the bottom surfaces. Finally, the solidification is completed near the bottom surface, because heat loss is mainly from the surrounding base metal.

The experimental samples are shown in figure 4. Different from the weld shape in gas tungsten arc welding

[13], the width of the top part in the weld is much greater than the interior fusion zone in figure 4(a) and 4(b) because the high-velocity, concentrated plasma arc pushes out much more high-temperature fluid in the process of PAW. The heating effect of high-temperature fluid increased the molten zone in the top. Comparing figures 2 and 3 with figure 4 indicates a reasonable agreement between the predicted and the experimentally observed fusion zone, shape and size. figure 4(c) shows the weld shape after burn through, helping us to understand the keyhole shape under the influence of the plasma arc. The cross section of the burn-through weld is nearly a hyperbolic shape, which agrees well with the predicted results.

Using the partial-penetration weld as an example, figure 5 shows the captured images of the top weld pool surface. According to the record on the video tape, the black zone surrounded by a grey circle could be used to approximate the molten pool. Because the axial direction of the image is compressed due to the location of LaserStrobe unit, the radial diameter, as shown in $t = 1.3$ s, is used to stand for the width of the weld pool. At $t = 2.0$ s, the solidification process began; the grey zone was increased at $t = 2.3$ s. At $t = 2.7$ s, a white spot appeared in the centre, suggesting that the solidification was completed. The comparison of the calculated and the experimental weld pool width is shown in figure 6. The weld pool width is determined by the radial diameter measured on the images multiplying a factor which is obtained according to the comparison of images (figure 4) and weld samples (figure 5). It is shown to be in good agreement, although the calculated pool width is a little smaller than the experimental width in the end. With the increasing size of the weld pool, the limited size of the calculation domain may affect the increase of the calculated pool width in the end.

5. Conclusion

A 2D heat and fluid flow model has been developed to analyse keyhole formation and collapse in stationary PAW.

The keyhole with a V-shape cross section in a partial-penetration weld and the keyhole with a hyperbolic-shape cross section in the full-penetration weld have been predicted and observed.

The weld pool oscillation could be triggered by the collapse of the molten pool. In the full-penetration weld, the addition of a free bottom surface results in a more significant weld pool oscillation, and the bottom and the top surface oscillation have close connections. The weld pool oscillation will continue until equilibrium or solidification is achieved.

The calculated temperature distribution during keyhole formation reveals that the highest temperature appears near the top of the molten pool. After the keyhole collapse, the fluid temperature around the periphery is lower than the temperature at the centre. Heat loss is mainly from the base metal. Thus, solidification is initiated at the solid–liquid interface and advances toward the centre. In the process of solidification, the higher temperature remains near the weld surface.

Acknowledgment

References

[1] Fuerschloach P W and Knorousky G A 1991 A study of melting efficiency in plasma arc and gas tungsten arc welding *Welding J.* **70** 287–97

[2] Solana P and OcaTHa J L 1997 A mathematical model for penetration laser welding as a free boundary problem *J. Phys. D: Appl. Phys.* **30** 1300

[3] Lampa C, Kaplan A F H, Powell J and Magnusson C 1997 An analytical thermodynamic model of laser welding *J. Phys. D: Appl. Phys.* **30** 1293

[4] Lankalapalli K N, Tu J F and Gartner M 1996 A model for estimating penetration depth of laser welding process *J. Phys. D: Appl. Phys.* **29** 1831

[5] Hsu Y F and Rubinsky B 1988 Two-dimensional heat transfer study on the keyhole plasma arc welding process *Int. J. Heat Mass Transfer* **31** 1409–21

[6] Keanini R G and Rubinsky B 1993 Three-dimensional simulation of the plasma arc welding process *Int. J. Heat Mass Transfer* **36** 3283–98

[7] Nichols B D, Hirt C W and Hotchkiss R S 1980 SOLA-VOF: a solution algorithm for transient fluid flow with multiple free boundaries *Report* LA-8355, Los Alamos Scientific Laboratory

[8] Metcalfe J C and Quigeley M B C 1975 Heat tranfer in plasma arc welding *Welding J.* **54** 535–85

[9] Haidar J 1998 Predictions of metal droplet formation in gas metal arc welding *J. Appl. Phys.* **84** 3530–40

[10] Kothe D B, Mjolsness R C and Torrey M D 1991 RIPPLE: a computer program for incompressible flows with free surfaces *Report* LA-12007-MS, Los Alamos Scientific Laboratory

[11] Goldak J, Bibby M, Moore J and Patel B 1986 Computer modelling of heat flow in welds *Metall. Trans.* B **17** 587–600

[12] Evans D W, Huang D, McClure J C and Nunes A C 1998 Arc efficiency of plasma arc welding *Welding J.* **77** 53–8

[13] Kim. W H, Fan H G and Na S J 1997 The effect of various driving forces on heat mass transfer in welding pool *Num. Heat Transfer* A **32** 633–52